

Chapter 1

Cooling and Trapping in a MOT

1.1 Chapter Outline

This chapter presents a description of the components of the experiment which are used to trap and cool atoms in a **mot!** (**mot!**). An outline of the hardware used to create both the 2D and 3D **mots!**s (**mots!**s) is presented in Section ???. Following this is a description of the μ Quans laser system, in Section ??, which generates the light used to cool and trap atoms. The hardware used to control the frequency and power of each **mot!** beam, as well as the required magnetic fields, is given in Section ??. Finally, this chapter concludes with a characterisation of the 3D **mot!** loading rate in Section ??

1.2 The Navigator Vacuum Chamber

The vacuum chamber, along with the components mounted to it, make up the majority of the hardware used in the preliminary trapping and cooling stages of the experiment. A diagram of the vacuum chamber and the main **mot!** components is shown

in Figure ???. The chamber is made of 316L stainless steel, which has a low magnetic permeability to reduce stray magnetic fields on the atoms during the experiment. It contains 16 DN40 ConFlat ports arranged on the edges of three octagons, one in each cartesian coordinate plane. Six of these ports provide optical access for the 3D **mot!**. Another port connects the 2D **mot!** system to the main chamber. One port provides optical access for either a CCD camera or photodiode. Opposite this is a microwave horn for driving microwave transitions between the two **rb87!** (**rb87!**) hyperfine ground states, The remaining DN16 ports are not used for optical access since they do not have a direct line of sight to the atoms. Instead, these are used to attach a pressure gauge, gate valve, a NexTorr NEG pump and electrical feedthroughs for the **mot!** coils. Two DN63 ports lie along one axis and are used to mount the optics for driving Raman transitions¹. This is the axis along which the atom interferometer is sensitive to accelerations, and will subsequently be referred to as the Raman axis.

The chamber is pumped down to a pressure of around 5×10^{-10} mbar using a NexTorr D100-5 pump. This is a composite system consisting of **neg!** (**neg!**) and an ion pump. The **neg!** is a porous sintered zirconium (St 172) element, which reacts with chemicals such as hydrogen, water, nitrogen, oxygen and hydrocarbons. Most of these were removed during the initial baking and roughing pump stages. Under **uhv!** (**uhv!**) conditions, the largest contributor to the pressure is hydrogen which the **neg!** can pump at a speed of 100 l s^{-1} . Any species that are not absorbed by the **neg!**, in particular Rubidium, are pumped by the 5 l s^{-1} ion pump.

1.2.1 The 2D MOT system

At the beginning of the project, atoms were loaded into the 3D **mot!** from background vapour. At room temperature, a large fraction of atoms have velocities greater than

¹For more information about the Raman optical system, refer to Section ??

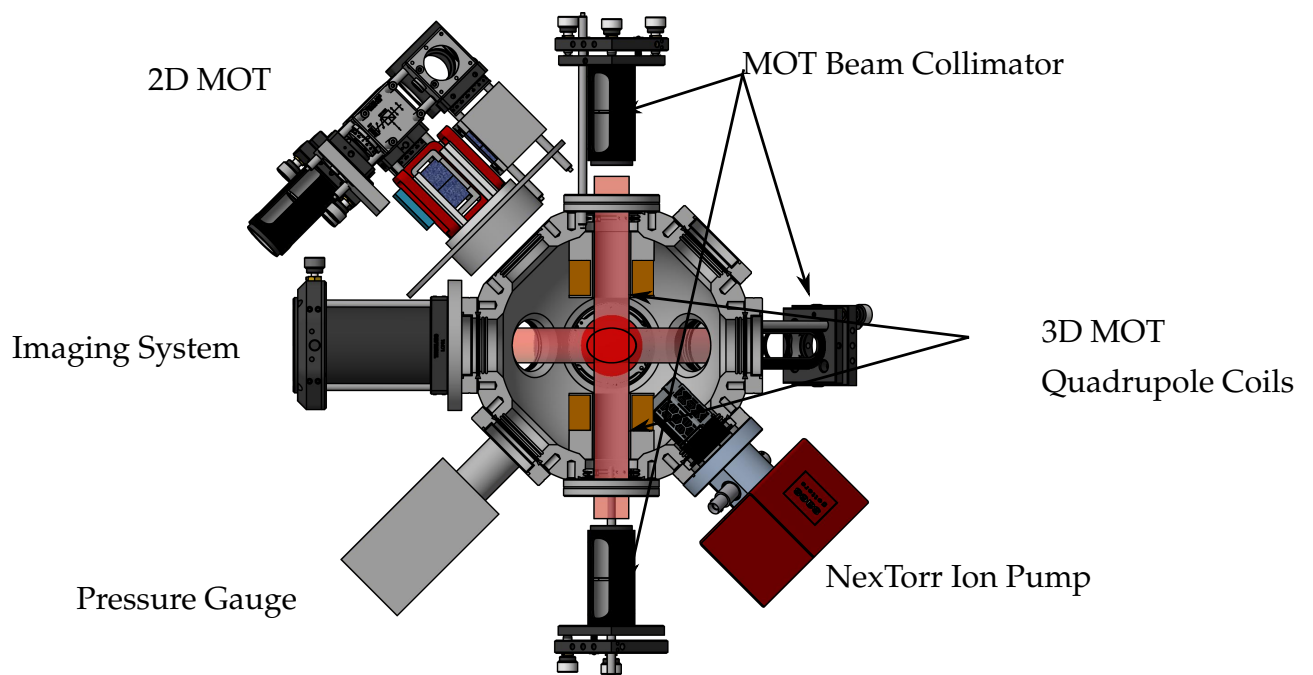


Figure 1.1: A diagram of the main components on the vacuum chamber used for the **mot!** systems. Rubidium atoms are dispensed and loaded into the 2D **mot!** before being pushed into the main chamber and collected in the 3D **mot!**. A set of 6 beam collimators provide the light necessary to slow and cool atoms, which are trapped using the spherical quadrupole field generated by the illustrated coils. Not shown are additional bias coils along each **mot!** beam axis to null stray fields at the centre of the chamber.

typical **mot!** capture velocities, so a very high partial pressure of Rubidium is needed to achieve a fast loading rate (see Section ??). This also contributes to a high background atom number, which reduces the interferometer fringe visibility. To increase the loading rate whilst decreasing the Rubidium partial pressure, a 2D **mot!** [Dieckmann1998] system was added to the experiment. This subsequently served as the atom source was for the 3D **mot!**.

A diagram of the light and magnetic fields required to produce a 2D **mot!** is presented in Figure ?. It is similar to the 3D **mot!**, with the main exception being that only 4 beams are used to cool the atoms along 2 orthogonal axes. It is designed to produce a large flux of cold atoms which can be subsequently loaded into a 3D **mot!**. The cooling beams are collimated to a large waist size and the magnetic field coils produce a cylindrical quadrupole field with a line of zero magnetic field along the axis of symmetry. Along this axis, the atoms are free to move, resulting in an atomic beam. This beam is collimated using a larger radial field gradient than is typically found in 3D **mot!** systems. This increases the radial confinement of atoms. In addition, a pinhole is placed at the exit of the cell, so that atoms with a high radial velocity will not leave the source cell. This pinhole also greatly reduces the conductance between the 2D **mot!** cell and the main chamber, which means that a high rubidium partial pressure can be maintained in the 2D **mot!** cell, without greatly increasing the pressure in the main chamber. The pinhole is drilled into a silicon plate, which partially reflects the beam that propagates along the central axis. This creates an unbalanced molasses that cools atoms with a large axial velocity. The scattering rate from each beam is not equal, so the net force on the atoms pushes them through the pinhole. By slowing a larger proportion of atoms to within the capture velocity of the 3D **mot!**, this configuration, referred to as a 2D+ **mot!**, loads a 3D **mot!** faster than the 4-beam counterpart.

A schematic of the optical components for the 2D **mot!** is presented in Figure ?. The

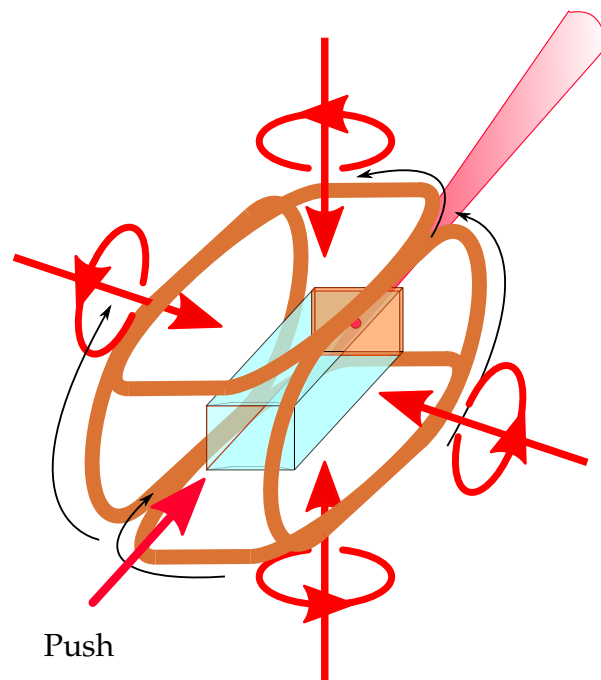


Figure 1.2: Schematic diagram for the 2D **mot!**. **rb87!** atoms are trapped and cooled along the 2 axes orthogonal to the long axis of the source cell. The black arrows indicate the direction of the current through each coil. Each circularly polarised beam drives σ_- transitions for an atom moving in the opposite direction. A linearly polarised push beam propagates along the longitudinal axis and is partially reflected by the silicon wafer at the opposite end. This provides a small amount of axial cooling and the imbalance of radiation pressure pushes atoms out of the cell. The pinhole at the other end prevents atoms with a high transverse velocity from leaving the cell.

cooling light originates from a single fibre, which is collimated to a beam waist of 9.5 mm using two aspheric lenses. This is then linearly polarised and divided into two beams of equal power using a **hwp!** (**hwp!**), one for each cooling axis. Each beam passes through a beam-splitter and a prism mirror, to increase the volume covered by the 2D **mot!** beams. A **qwp!** (**qwp!**) circularly polarises the beam before it enters the ar-coated glass cell. On the opposing side of the cell, a 25 mm \times 35 mm mirror retro-reflects the beam. This is coated with a layer of quartz to form a **qwp!**, so that the reflected beam has the same polarisation handedness as the incoming. The push beam originates from a second fibre input. A fixed focus collimator collimates the beam to a waist of 1.5 mm. This is mounted onto a 1 in kinematic mount to align the push beam to the 0.7 mm pinhole at the other end of the cell. The push beam is linearly polarised by a **pbs!** (**pbs!**) to reduce the effect of polarisation drift on the axial cooling of the 2D **mot!**. The cell, manufactured by ColdQuanta, has dimensions of 30 mm \times 30 mm \times 44 mm and is specifically designed for creating a 2D **mot!**. It contains two rubidium dispensers composed of rubidium chromate (RbCrO_4) and a reducing agent. These were activated by passing a large current through them to remove a thin oxidation layer. To produce rubidium, a current of around 2.8 A is passed through the dispenser to trigger an electro-chemical reduction reaction, so that pure rubidium sublimates.

The cylindrical quadrupole field is generated by a set of coils that are manufactured by ColdQuanta. They are mounted so that the axis of zero magnetic field coincides with the central longitudinal axis of the source cell. These produce a radial field gradient per current of $20 \text{ G cm}^{-1} \text{ A}^{-1}$. A simulation of the field gradient along each axis, along with the magnetic field in each plane of symmetry is shown in Figure ?? . Across the centre of the cell, the field gradient is very uniform. The equilibrium position where the **mot!** (**mot!**) forms is adjusted using Helmholtz coil pairs along each **mot!** axis. These coils produce a field per current of 1 G A^{-1} .

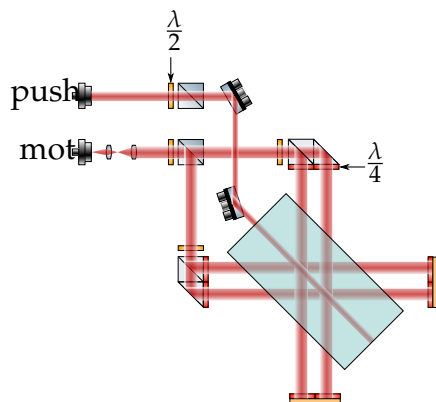


Figure 1.3: Optical components for the 2D **mot!**. The light for the **mot!** is split into two equal portions using a **hwp!** and **pbs!**. Along each axis, the beam passes through a **pbs!** and a prism mirror to increase its spatial extent. The beam is circularly polarised before entering the cell and retro-reflected by a mirror coated with a **qwp!**. The push beam is collimated from another fibre input and linearly polarised before entering the cell along the longitudinal axis.

1.2.2 The 3D MOT system

The main chamber contains the apparatus that is used to make a 3D **mot!**. Each **mot!** beam originates from a **pm!** (**pm!**) fibre and is collimated using a lens with a nominal focal length of 75 mm to a waist size of 7.5 mm. At the output of each collimator is a **qwp!**, with its slow axis oriented at a 45° angle to either the fast or slow axis of the fibre, to produce either left- or right-handed circularly polarised light. The **mot!** beams along the axial direction of the quadrupole field (i.e. the \vec{z} direction) are orthogonally polarised to the others along the \vec{x} and \vec{y} directions. The **mot!** beams are aligned so that their intensities at the centre of the chamber are equal, so that the **mot!** forms where the magnetic field is zero.

Spherical quadrupole magnetic field

The magnetic field for the 3D **mot!** is created by a pair of coils in an anti-Helmholtz configuration. Each coil is wound using rectangular wire coated in a $35\ \mu\text{m}$ thick layer of Pyre-M.L, a UHV-compatible polyamide which provides a layer of insulation

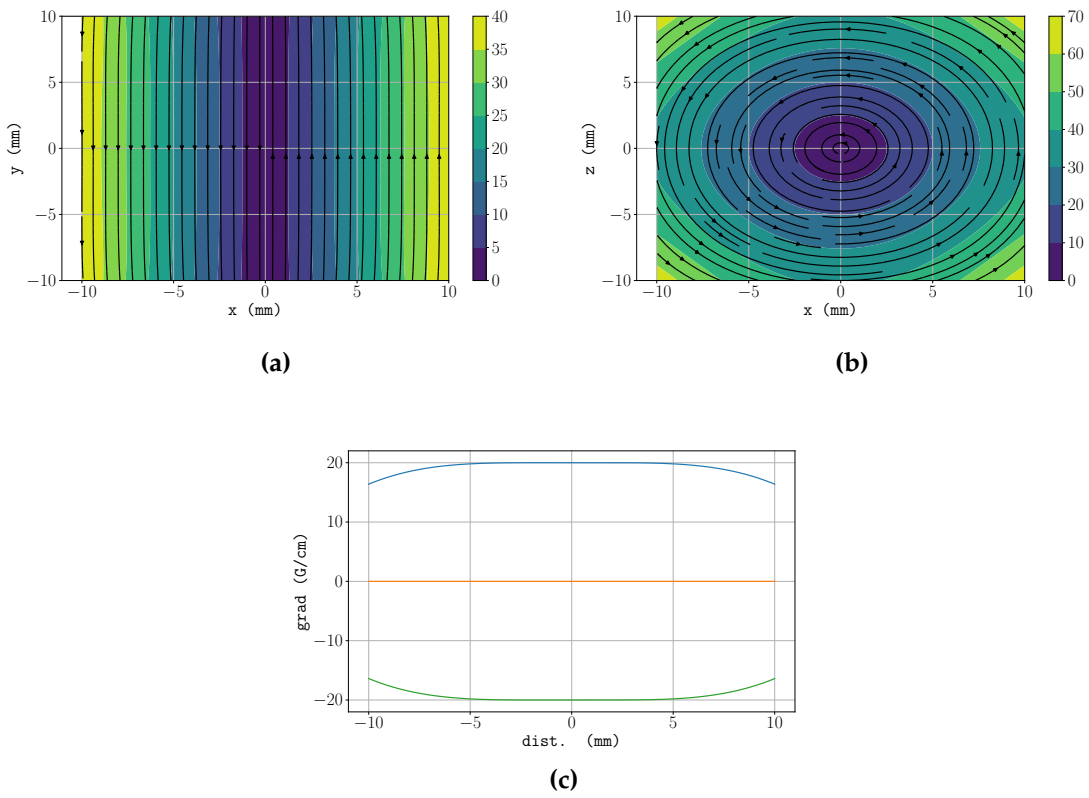


Figure 1.4: Simulated field and field gradients for the 2D **mot!** quadrupole coils. In this coordinate system, the 2D **mot!** cools and traps atoms in the \vec{x} and \vec{z} directions. The simulation was performed using a nominal current of 1 A, which corresponds to a current density in each coil of 7.78 A mm^{-2} . The magnitude of the magnetic field (in units of G) and its direction in the axial and radial planes of symmetry are shown in (a) and (b), respectively. (c) shows the field gradient components $\partial_x B_x$ (blue), $\partial_y B_y$ (orange) and $\partial_z B_z$ (green) along their corresponding axes.

between each loop. The wire has a cross-section of dimensions $1.1 \text{ mm} \times 1.1 \text{ mm}$, with 20 axial loops and 12 radial loops. The inner diameter of the coil is 25.4 mm, to allow for optical access of the \vec{z} -axis **mot!** beams, and the maximum diameter is 59.2 mm – small enough that the coil could be inserted into the chamber through the DN63 CF ports. The coils are mounted to the chamber using groove grabbers which clamp into grooves inside the wall of the DN40 ports. The coil formers increase the surface area in contact with the chamber, increasing the rate of heat dissipation from the coils. A plot of the measured temperature over time is given in Figure ?? both at atmospheric pressure and inside the chamber. At a pressure of around 10^{-2} mbar, the temperature of the coils inside the chamber does not exceed 40°C . Once mounted, the distance between the innermost loops is 70 mm. Figure ?? shows the magnetic field, measured using a Hall probe, along the axis of symmetry for each of the coils with a current of 2.53 A. Figure ?? shows the axial field measured when the coils are in anti-helmholtz configuration. These are in close agreement with a simulation of the magnetic field. The simulated field in the axial and radial planes of symmetry are shown in Figure ?? and Figure ??, respectively.

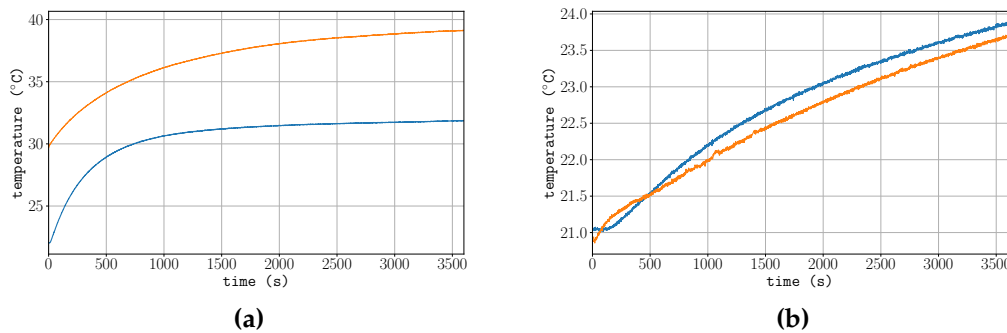


Figure 1.5: Temperature rise due to the **mot!** coils over 1 hour of operation. The blue curves were measured when the coils were at atmosphere and the orange were measured under a rough vacuum around 10^{-2} mbar. (a) shows the temperature of the coils and (b) is the temperature of the exterior of the chamber.

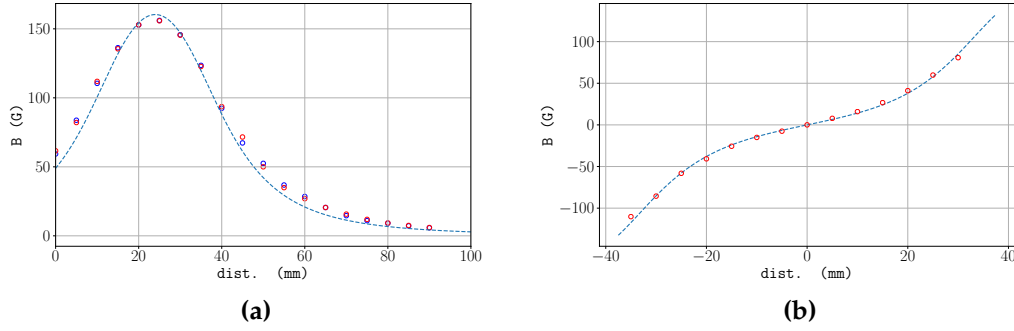


Figure 1.6: Measured magnetic field and field gradient for the 3D **mot!** coils. **(a)** shows the axial magnetic field for the two coils as measured using a Hall probe. **(b)** shows the field close to the centre when the coils are in an anti-helmholtz configuration. The dashed lines indicate the axial field as calculated from the simulation shown in Figure ??.

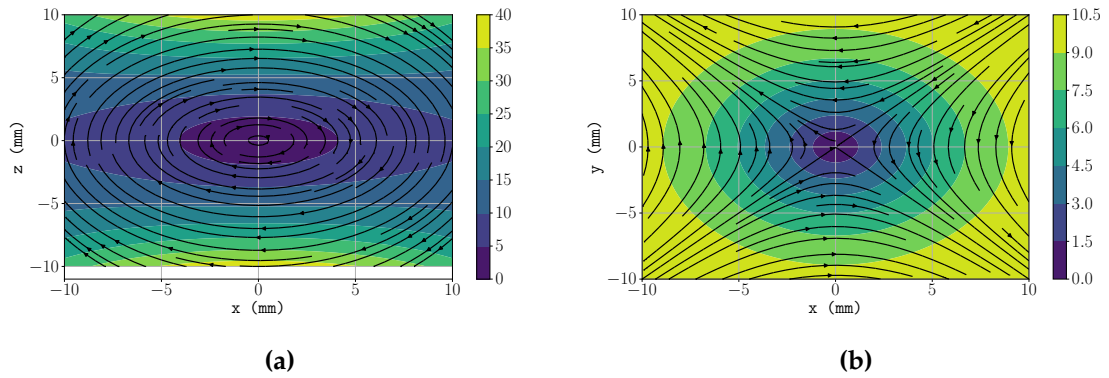


Figure 1.7: Simulated magnetic field for the 3D **mot!** quadrupole coils. In this coordinate system, the axial direction is defined as the \vec{z} axis. The simulation was performed using a nominal current of 2.53 A, which corresponds to a current density in each coil of 1.33 A mm^{-2} . The magnitude of the magnetic field (in units of G) and its direction in the axial and radial planes of symmetry are shown in **(a)** and **(b)**, respectively.

Axis	a (mm)	r_i (mm)	r_o (mm)
\vec{x}	88	105	115
\vec{y}	132	178	188
\vec{z}	116	123	133

Table 1.1: Table of parameters for each 3D **mot** !bias coil. a denotes the axial separation between each coil, r_i and r_o are the inner and outer radii.

Bias Coils

Three orthogonally arranged pairs of Helmholtz coils are used during the experiment to provide a homogeneous magnetic field close to the centre of the chamber. In the initial loading and molasses stages, these are used to zero the magnetic field at the centre of the chamber. This is required for effective sub-Doppler cooling . In subsequent stages, these coils provide a bias field along the appropriate axes during state preparation, interferometry and state detection. Each coil was wound using 1 mm thick wire and consisted of 5 axial and 10 radial turns. For a pair of coils in Helmholtz configuration, the magnetic field gradient at the centre is minimised when the axial separation a is equal to the coil radius r , but the geometry of the vacuum chamber meant that it was not possible to satisfy this condition. The radii and axial separations of each coil pair is presented in Table ??.

1.2.3 CCD Imaging

During the experiment, atoms are imaged using a CCD camera to spatially resolve the cloud. This was done to measure the temperature using a ballistic expansion method and the trajectory of the cloud (see Section ??). Figure ?? shows a diagram of the apparatus used for imaging. A pair of 125 mm and 50 mm focal length lenses are used to image the cloud onto a Pike F505-B CCD camera. The camera has a maximum

resolution of 2452×2054 pixels. A measurement of the magnification of a ruler gave a calibration factor of 7.065(70) pixel/mm. To reduce the level of background light on the CCD, a bandpass filter is placed in front of the sensor. This transmits 780 nm light at an efficiency of 60%.

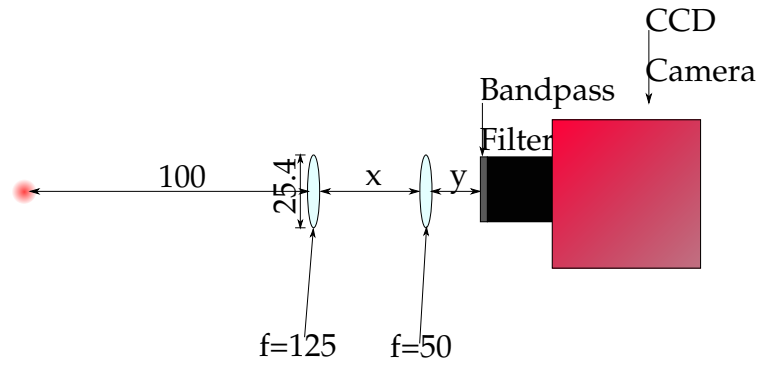


Figure 1.8: Optical setup for CCD imaging. Two lenses are used to magnify the image of the atom cloud on the CCD. A bandpass filter is placed in front of the sensor to block out background light at wavelengths other than 780 nm. All lengths are given in millimetres.

Incident Optical Power Calibration

Measuring the incident optical power is useful for estimating the number of atoms N_a by measuring the amount of light emitted during resonance fluorescence. However, typical number densities in a **mot!** mean that incident light is strongly absorbed by atoms close to the surface. Consequently, the assumption of a constant scattering rate per atom is not valid and leads to an under-estimate of the atom number. More accurate techniques such as absorption imaging can be used, but for the purposes of this experiment, it was sufficient to use fluorescence imaging as a rough estimate of the number of atoms in the **mot!**. In subsequent stages of the experiment, a sensitive photodiode with a high bandwidth was used to detect the atoms in each hyperfine ground state. Details on this setup can be found in Section ??.

Under the assumption that the power radiated per atom is constant, the power incident on the CCD P_{ccd} can be related to the scattering rate per atom as follows

$$P_{\text{ccd}} = \frac{\Omega}{4\pi} t R_{\text{sc}} \hbar \omega N_a \quad (1.1)$$

where $\Omega/4\pi = 1.8 \times 10^{-3}$ is the fractional solid angle subtended by the imaging optics, t is the transmission of the bandpass filter, R_{sc} is the scattering rate as previously defined in equation (??) and $\hbar \omega = 1.6 \text{ eV}$ is the emitted photon energy. This incident power is then related to the integrated number of pixel counts C_{int} by

$$C_{\text{int}} = \alpha \tau_{\text{exp}} \eta P_{\text{ccd}} \quad (1.2)$$

where τ_{exp} is the exposure time, $\eta = 0.14$ is the quantum efficiency of the CCD and α is a scaling factor that relates the total charge collected to the total number of pixel counts. By varying the exposure time used to image a collimated beam with a total power of $0.17 \mu\text{W}$, the total number of counts recorded by the camera as a function of exposure time is plotted in Figure ???. This gives a count scaling factor of $\alpha = 2.2 \times 10^5 \text{ counts } \mu\text{s}^{-1} \mu\text{W}^{-1}$.

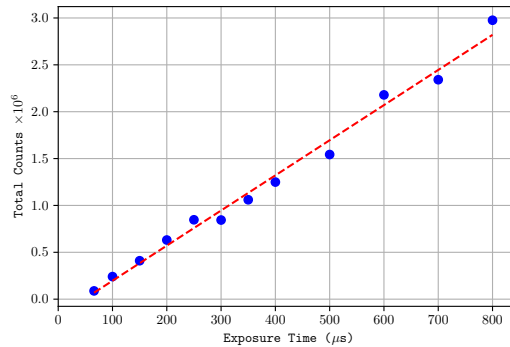


Figure 1.9: Integrated pixel counts as a function of CCD exposure time for an incident optical power of $0.17 \mu\text{W}$. The dashed line indicates a linear regression which gives a scaling factor of $\alpha = 2.2 \times 10^5 \text{ counts } \mu\text{s}^{-1} \mu\text{W}^{-1}$.

1.3 Generating MOT light

All the **mot!** light in this experiment was generated by the μ Quans laser [**muquansWebPage**]. μ Quans is a French laser company that is a spin-off from the Institut d'Optique and Observatoire de Paris. A schematic of this laser system is shown in Figure ???. The light is fibre-coupled to minimise the number of free-space optical components. This makes the system more stable in the presence of vibrations and temperature variations. The μ Quans laser is comprised of four 1560 nm **ecd!**s (**ecd!**s) which are frequency-doubled to produce light at 780 nm. The first acts as a master laser which is locked to the $|F = 3\rangle \rightarrow |F' = 3, 4\rangle$ crossover point in **rb85!** (**rb85!**) to serve as an absolute frequency reference. The other three slave lasers are used for output. The first one provides light for cooling **rb87!** using the $|F = 2\rangle \rightarrow |F' = 3\rangle$ transition. Light for the $|F = 1\rangle \rightarrow |F' = 2\rangle$ repump transition is created by phase modulating this laser using an **eom!** (**eom!**). The other two make up a pair of lasers for driving Raman transitions. One laser is frequency-offset locked to the master and the other is phase-locked to the first. This Raman laser was not used in this experiment, so will not be discussed in further detail. The power in each of these slave lasers is amplified using an **edfa!** (**edfa!**). The frequency is doubled to around 780 nm using a **ppln!** (**ppln!**). The output power is controlled using an **aom!** (**aom!**).

1.3.1 Absolute Frequency Reference

The master laser provides an absolute frequency to which the slave lasers are offset-locked. The reference frequency is created using saturated absorption spectroscopy inside a Rubidium vapour cell. The sub-Doppler features in this spectrum are insensitive to temperature changes, and under have linewidths closer to the natural linewidth of Rubidium ($\Gamma \sim 2\pi \times 6$ MHz). Figure ??? shows the saturated absorption

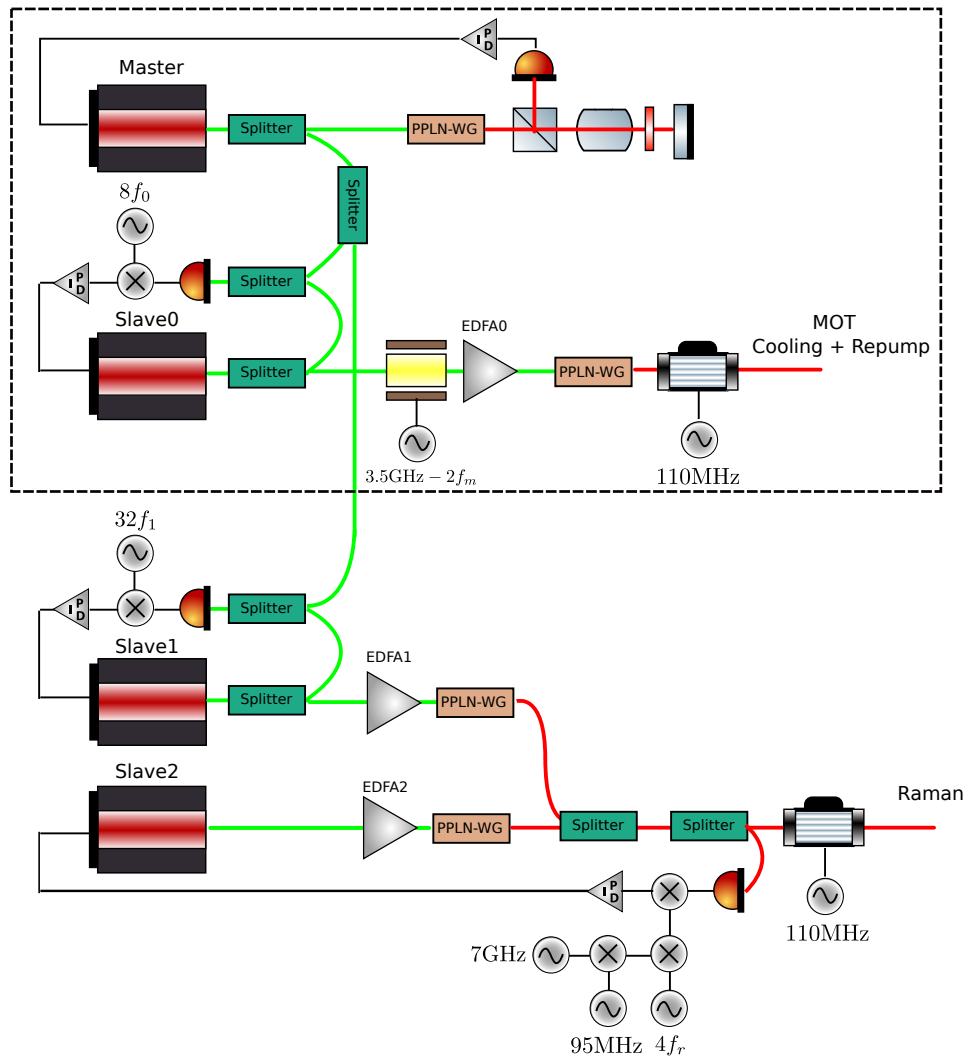


Figure 1.10: Schematic of the μ Quans laser system. Each output laser is derived from a 1560 nm **edfa!** (shown in green) which is amplified using an **edfa!** and then frequency-doubled to 780 nm using a **ppln!** crystal. A master laser is locked to the 3,4 crossover in **rb85!** and the output lasers are offset-locked to their corresponding frequencies. The dashed region indicates the components used for generating light for the **mots!**s, which was the only function of this laser for this experiment.

spectrum using the μ Quans master laser. The frequency is varied by finely adjusting the temperature of the master **ecl**!. The master laser is set to lock to the crossover resonance between the $F = 3 \rightarrow F' = 3$ and $F = 3 \rightarrow F' = 4$ transitions in **rb85**! (indicated as **(b)**), which is the strongest feature in the spectrum. This absorption feature is around 1.1 GHz below the cooling transition in **rb87**! (indicated as **(a)**). The

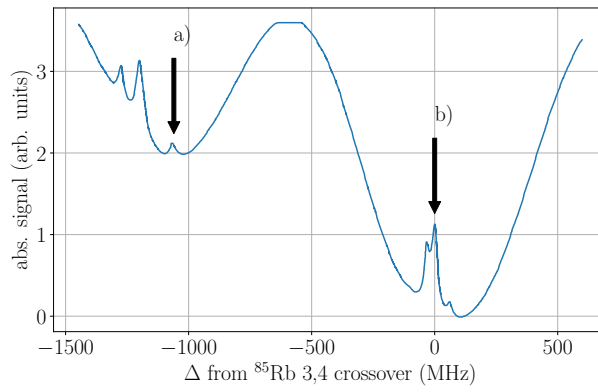


Figure 1.11: Saturated absorption spectroscopy using the Rubidium vapour cell in the μ Quans laser. The absorption features indicated are *a*: the $F = 2 \rightarrow F' = 3$ transition in **rb87**! and *b*: the crossover resonance between the $F = 3 \rightarrow F' = 3$ and $F = 3 \rightarrow F' = 4$ transitions in **rb85**! which is used to lock the frequency of the master laser.

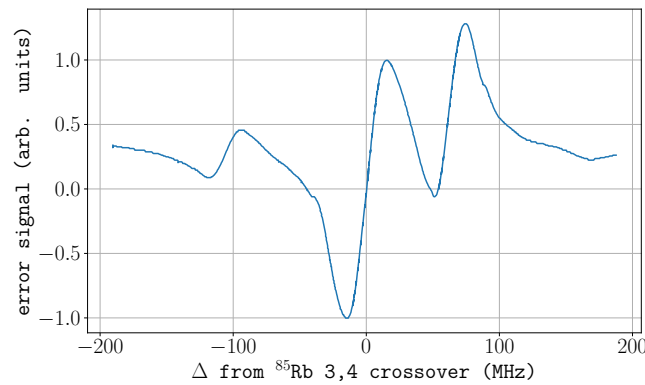


Figure 1.12: Error signal obtained by modulating the laser current. Close to the lock point, the signal is approximately linear. This signal is used in a feed-back loop to correct for frequency changes of the master laser.

frequency of the laser is modulated by modulating the current to the **ecl**! (**ecl**!). This produces a signal that is proportional to the frequency difference from the lock

point. The error signal shown in Figure ?? is obtained by demodulating the absorption signal using a lock-in amplifier. The servo that controls the master laser frequency also contains an integrator to compensate for long-term drifts arising from temperature variations.

1.3.2 Cooling and Repump Light

The first of the slave lasers provides light to address the cooling transition. This is frequency-offset locked to the master by comparing their beat frequency to a reference from a **dds!** (**dds!**). A plot of the error signal used to lock this offset frequency is shown in Figure ??.

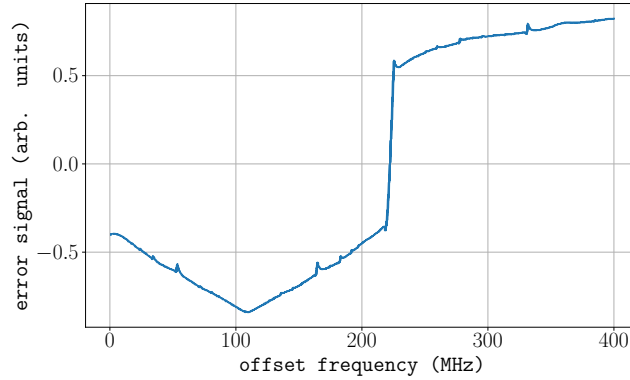


Figure 1.13: Error signal for the μ Quans cooling laser, plotted as a frequency difference from the start of the scan. This is obtained by comparing the beat frequency between the master and slave lasers to a reference frequency generated by a **dds!**. A servo loop feeds-back onto the frequency of the slave laser to keep this difference close to zero.

An **eom!** modulates the phase of the cooling laser to produce light for the $|F = 1\rangle \rightarrow |F' = 2\rangle$ repump transition. This modulation creates frequency sidebands separated by integer multiples of the modulation frequency f_m . If the amplitude of the modulation is small, only the first positive and negative sidebands are present. A separate **dds!** provides the reference for the modulation frequency, so that the frequency of the

cooling and repump light can be independently ramped during the experiment (see Section ??). This is amplified, doubled and subtracted from a 3.5 GHz reference signal so that the positive frequency sideband is approximately 6.6 GHz above that of the cooling light, to address the repump transition. The modulation power is externally controlled using a **vca!** (**vca!**) to control the ratio of repump power to cooling power. An RF switch turns the repump on and off by blocking the reference frequency.

The total output power is controlled using an **aom!** that has a fixed modulation frequency of 110 MHz. Similarly to the repump **eom!**, this modulation signal also has a **vca!** and RF switch to control the power and state of the output.

1.3.3 Real-Time Control

During the experiment, it is necessary to vary the frequency and power of both the cooling and repump light. Analogue and digital signals control the RF sources for the output **aom!** and **eom!**. A **dds!** generates each RF frequency, so that they can be updated in real-time. These are also programmed to ramp the output frequency for a specified duration and ramp rate. This is done by sending serial messages to an application which interprets the message and synchronously communicates the command to the **dds!** using SPI. A glossary of the messages and their function is given in Appendix ?. The command is stored in memory on-board the **dds!** and is triggered to start using a digital pulse. This means that time at which the frequency of the light changes is synchronised with the rest of the experiment.

1.4 Controlling the MOTs

Effective trapping and cooling of Rubidium requires careful control of the light and magnetic fields used to create the **mot!**. A well-balanced **mot!** requires circularly polarised beams with equal intensities so that there is no net force from scattering light. Otherwise, the **mot!** forms at a position where the magnetic field is not zero [Steane1992]. Equivalently, the **mot!** requires good control of the magnetic field inside the chamber. What follows is a description of the hardware used to implement this control. Section ?? describes the network of optical fibres used to control the frequency and power in each **mot!** beam. The electrical circuits used to control the strength of each bias field, as well as switching off the quadrupole coils, are described in Section ??

1.4.1 Optical Fibre Network

A network of fibre-based beam-splitters and **aoms!**s (**aoms!**s) distributes the light from the μ Quans fibre to each of the beams for the 2D and 3D **mots!**s. This provides independent control of the power and frequency of the light at each output of the fibre network. A diagram of this setup is shown in Figure ?. The μ Quans fibre output is polarised using a polarising beam-splitter before a **hwp!** aligns it with the slow axis of a **pm!** fibre. The light is first divided on a 1:2 beam-splitter, with 66% exiting one port, used for the 3D **mot!**. The 34% on the other port is split again using another 1:2 beam-splitter so that 95% and 5% of the power exits each port, for the 2D **mot!** and push beam, respectively. Independent control each output is done using a *Gooch and Housego* fibre **aoms!**s with a central modulation frequency of 135 MHz. The junctions between components are spliced together to minimise insertion loss. The slow axes of each fibre are aligned so that the polarisation of the input light is maintained.

The light for the 3D **mot!** is split using a 1:3 splitter into pairs of outputs for the light along the \vec{x} , \vec{y} and \vec{z} axes. Unlike the outputs along the other axes, the ones used for light along the \vec{z} axis have separate **aoms!**. This is done so that during the experiment, a single beam along the \vec{z} axis can be used to blow away background atoms (see Section ?? for more details).

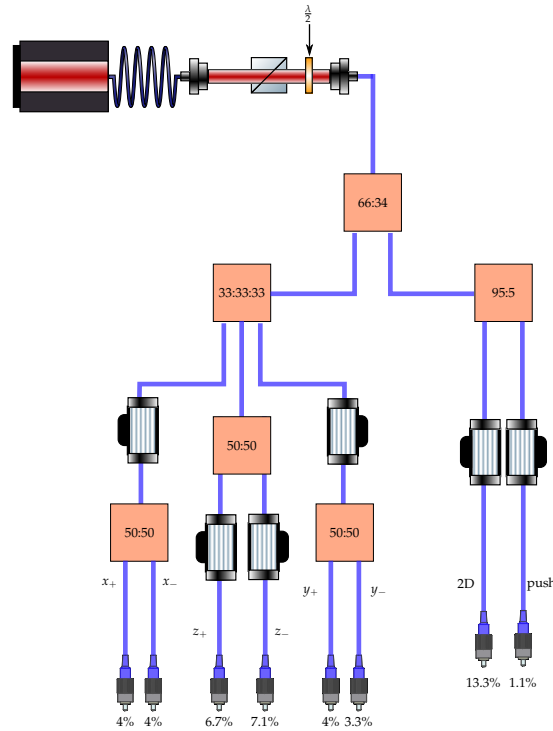


Figure 1.14: Fibre splitter and **aoms!** for **MOT!** light distribution. The polarisation of the cooling and repump light from the μ Quans laser is aligned to the fibre network using a **pbs!** and **hwp!**. Apart from the outputs for the \vec{x} and \vec{y} 3D **mot!** beams, which have a single **aom!** per axis, the power and frequency at each output can be controlled independently. The percentages shown are the relative power at each output, accounting for insertion loss and driving each **aom!** with the optimum RF power.

1.4.2 Magnetic Field Control

The current through each set of bias coils (3 for the 3D **mot!** and 2 for the 2D **mot!**) is controlled using a voltage-controlled current source. The control voltage is an input at the non-inverting terminal of an OPA549 op-amp. The coils are placed in series

with a sense resistor of resistance R_s at the output. The circuit is configured so that the voltage at the inverting terminal is $V_- = iR_s$. This forms a negative feedback loop to keep the output current constant if the load resistance changes. The bias coils can be supplied with up to 2 A using a control voltage of 10 V.

This same circuit is used to control the 3D **mot** coils, except for the fact that their larger resistance necessitates a larger gain to achieve the current necessary to produce a strong field gradient. During the experiment, the 3D **mot** coils need to be switched off rapidly, to allow for effective sub-Doppler cooling of the atoms. The coils are an inductive load, so the time taken for the current to decay is determined by the time constant $\tau = L/R$. With a negative voltage across them, the stored energy (and hence, magnetic field) dissipates at a faster rate. A flux-gate magnetometer was used to measure the time taken to switch off the coils. With an applied voltage of 0 V, the characteristic decay time is $\tau = 2.5$ ms. Under the maximum available back-EMF of -24 V, the field can be completely switched off in $800 \mu\text{s}$.

The quadrupole coils for the 2D **mot** are switched off in much the same way. An IGBT cuts the flow of current when the gate voltage drops below a threshold value. To prevent damage to the transistor, a diode and 10Ω power resistor are placed in parallel with the coils. This allows the current generated by the back-EMF to dissipate without damaging the IGBT. These fields from these coils can be switched off in less than 1 ms.

1.5 Characterising the MOTs

This section discusses the performance of the 2D and 3D **mot**s for trapping and cooling **atoms**!. The main goal of this stage of the experiment is to quickly produce an ensemble of trapped, cold atoms in the 3D **mot**!. For this reason, the loading rate of

the 3D **mot!** is a useful figure-of-merit. As further cooling in an optical molasses is necessary to achieve a sufficiently cold ensemble for interferometry (see Section ??), the temperature of atoms in the **mot!** will not be discussed in detail.

At the start of the experiment, the light and magnetic fields to produce the 2D and 3D **mots!** are switched on. Table ?? shows typical values for the cooling and repump power, as well as the field gradients and bias fields used. The cooling light is detuned by -2Γ from the $|F = 2\rangle \rightarrow |F' = 3\rangle$ transition for the 2D **mot!** and by -2.5Γ for the 3D **mot!**. The push beam is at resonance. A timing diagram of the loading sequence is given in Figure ?. The light and magnetic fields for the 2D **mot!** are switched off after 100 ms and the 3D **mot!** is kept on for a further 50 ms to allow for the transit of the remaining atoms from the 2D **mot!** to the 3D **mot!**. After a sufficient number of atoms are loaded, the experiment proceeds by switching off the 3D quadrupole field prior to cooling in an optical molasses.

2D MOT				3D MOT			
Laser Power		Magnetic Field		Laser Power		Magnetic Field	
Cooling	60 mW	$d\vec{B}/d\rho$	18 G cm^{-1}	Cooling	130 mW	$d\vec{B}/dz$	15 G cm^{-1}
Repump	6 mW	B_x	0.48 G	Repump	13 mW	B_x	1 G
Push	500 μW	B_y	-0.46 G			B_y	-0.5 G
						B_z	0.22 G

Table 1.2: Typical optical and magnetic parameters used for the 2D and 3D **mots!**. The optical powers listed are the total used for each **mot!**, which is divided into separate beams. The bias field strengths are the values used during the preliminary trapping stage of the experiment. The specified field gradients are given along the radial direction and the symmetry axis of the quadrupole coils for the 2D and 3D **mots!**, respectively.

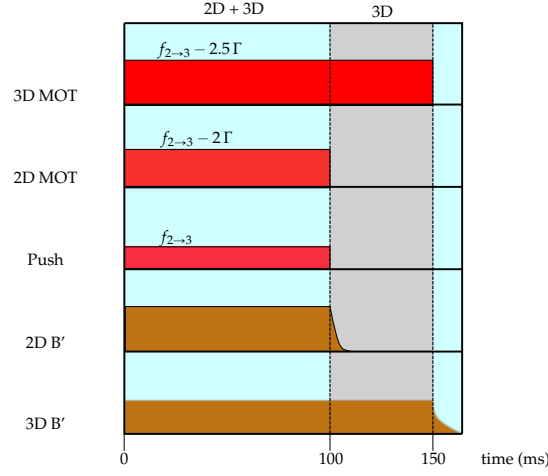


Figure 1.15: Timing diagram for the loading stage of the experiment. The 2D **mot!** is switched on for 100 ms and is switched off earlier than the 3D **mot!**.

1.5.1 3D MOT Loading Rate

The loading rate of the 3D **mot!** from a beam of atoms originating from the 2D **mot!** can be understood using the following rate equation

$$\frac{dN}{dt} = R\phi_{rb} - (\alpha\phi_{rb} + \beta n_{bg}) N - \gamma N^2 \quad (1.3)$$

where ϕ_{rb} is the flux of rubidium through 3D **mot!** capture volume and R describes the rate at which rubidium is cooled and trapped such that $R\phi_{rb}$ is the loading rate of the 3D **mot!**. The second term describes a loss rate due to collisions between trapped atoms and untrapped rubidium and background atoms. These loss rates are parameterised by α and β , respectively. The final term describes the loss of atoms from the trap due to intra-trap collisions [Prentiss1988] which depends on the density of atoms in the trap. In the case of a large flux of atoms from the 2D **mot!** the first two terms dominate, leading to a simple solution for the number of atoms in the 3D **mot!**

$$N(t) = \frac{R\phi_{rb} \left(1 - e^{-t(\beta n_{bg} + \alpha\phi_{rb})} \right)}{\beta n_{bg} + \alpha\phi_{rb}} \quad (1.4)$$

which has a steady-state atom number given by

$$N_{\infty} = \frac{R\phi_{\text{rb}}}{\beta n_{\text{bg}} + \alpha\phi_{\text{rb}}} \quad (1.5)$$

Under a small atomic flux, both the loading rate and steady-state atom number increase as the flux of atoms from the 2D **mot!** increases. Once this flux is great enough, the loss due to background atom collisions is small compared to the loss due to rubidium collisions and the final number is independent of ϕ_{rb} .

The flux of atoms from the 2D **mot!** depends on the 2D **mot!** loading rate, which in turn depends on the capture volume and rubidium number density inside the cell. Without any longitudinal cooling, a significant fraction of atoms leaving the cell will have a velocity greater than the 3D **mot!** capture velocity [Schoser2002].

The effect of varying the partial pressure of rubidium inside the source cell is shown in Figure ?? . The number of atoms in the 3D **mot!** was measured over time for a range of dispenser currents. At low partial pressures, the loading rate increases due to the increase in the flux from the 2D **mot!**. As the pressure increases, the increasing flux gives a larger steady-state number of atoms, up until the background pressure becomes negligible. Figure ?? and Figure ?? compare the loading curves observed with and without the push beam. Below a threshold pressure, the push beam greatly improves the loading rate since a greater fraction of the atoms can be captured in the 3D **mot!**.

Figure ?? shows the fitted loading rate for each scenario. There is a clear optimum pressure, where the loading rate is $2.4 \times 10^9 \text{ s}^{-1}$. The steady-state atom number is independent of the flux from the 2D **mot!**. Above this pressure, the loading rate is sharply reduced. The increased collision rate between cold atoms from the 2D **mot!** and hot untrapped ones reduces the atomic flux. This also increases the mean velocity

of atoms in the beam, since faster ones are less likely to collide with a background atom before exiting the cell. At very high pressures, the mean velocity is so great that only a small fraction of atoms can be captured and the push beam has little effect on the loading rate.

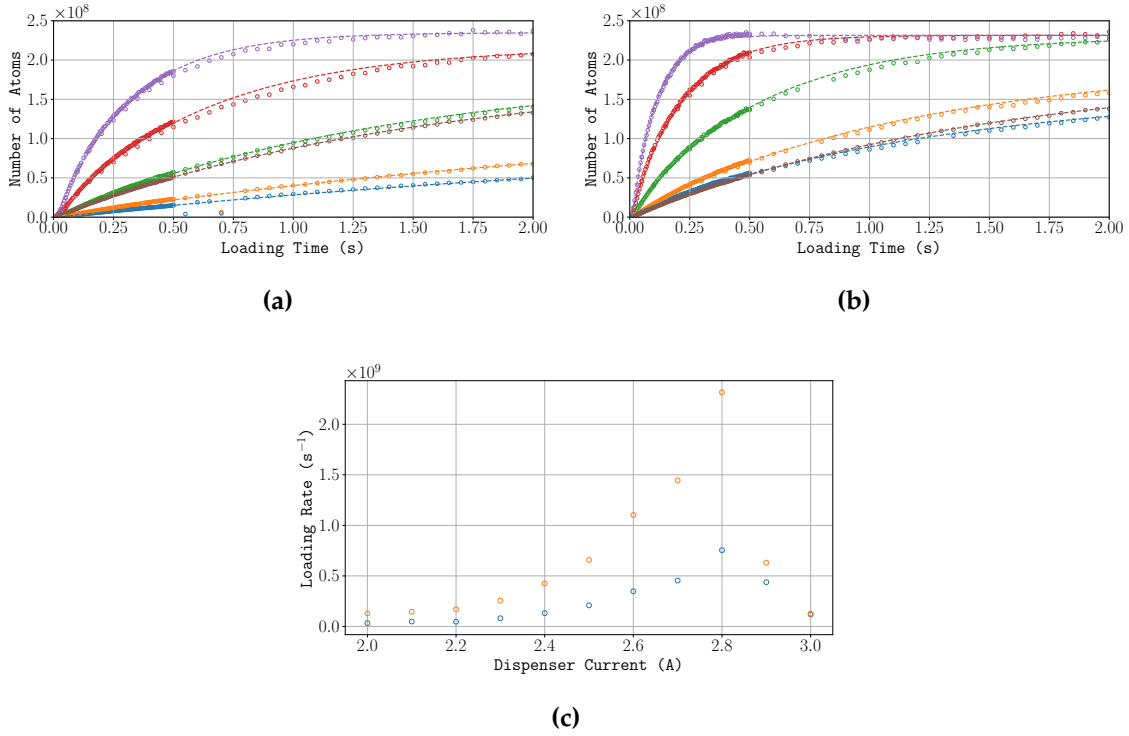


Figure 1.16: Number of atoms in the 3D **mot!** over time for a range of dispenser currents. For clarity, only the loading curves for dispenser currents of 2 A (blue), 2.2 A (orange), 2.4 A (green), 2.6 A (red), 2.8 A (purple) and 3 A (brown) are shown in (a) and (b), which present the number of atoms over time without and with a push beam, respectively. The loading rate ($R\phi_{\text{rb}}$ in equation (??)) in both instances is shown in (c). As the partial pressure of rubidium increases, the flux of atoms from the source cell increases. By longitudinally cooling the atoms, the push beam enhances the loading rate of the 3D **mot!**. Above a dispenser current of 2.8 A, the collision rate with hot untrapped atoms greatly reduces the atom flux, reducing both the loading rate and steady-state atom number.

1.6 Conclusion

This chapter has introduced the components of the experiment that were used to trap and cool atoms in a **mot!**. This is used to prepare an ensemble of cold atoms in a pure quantum state, suitable for interferometry. An optimisation of the loading rate of the 3D **mot!** was carried out to reduce the dead time between consecutive experiment cycles.

